Journal of Geodesy (2025) 99:78
https://doi.org/10.1007/s00190-025-01998-8

ORIGINAL ARTICLE

Gravity field recovery based on GNSS data of nano-satellites: a case study for the Spire CubeSat constellation

Thomas Grombein[1] · **Daniel Arnold**[2] · **Martin Lasser**[2] · **Adrian Jäggi**[2]

Received: 15 February 2025 / Accepted: 15 August 2025
© The Author(s) 2025

Abstract
A growing number of Low Earth Orbiting (LEO) satellites are collecting GNSS tracking data that allows to recover the long-wavelength part of the Earth's time-variable gravity field. Besides scientific LEO missions, commercial satellite constellations consisting of a huge number of nano-satellites are moving into focus. Due to an improved ground track coverage, such constellations offer the opportunity to increase the spatio-temporal resolution of derived gravity field models and can contribute to reduce temporal aliasing errors of dedicated gravity field missions. The Spire constellation is of particular interest as it consists of more than 100 nano-satellites (standardized CubeSats), all equipped with high-quality GNSS receivers. Furthermore, the Spire constellation offers a variety of orbital characteristics with different inclinations at altitudes of about 400–650 km. In this study, we use GNSS data from nine Spire CubeSats to derive monthly gravity field solutions covering a six-month period. The orbit and gravity field recovery is performed with the Bernese GNSS Software, which applies the Celestial Mechanics Approach. We demonstrate that the 2–3 times larger noise level of the Spire GNSS observations affects the quality of the retrieved gravity field solutions in the same order of magnitude. Therefore, a single Spire CubeSat solution cannot compete with those obtained from scientific LEO missions. However, with an increasing number of CubeSats, the performance improves so that a combination based on data from all nine Spire CubeSats can achieve a quality level comparable to a solution derived from ESA's Swarm-B satellite.

Keywords Gravity field · HL-SST · Spire · CubeSats · GNSS · Kinematic orbits

1 Introduction

By observing the time-variable gravity field with satellites, mass transport and redistribution processes in the Earth system can be monitored on global to regional scales. These spatio-temporal mass changes are connected to various components of the climate system, such as the atmosphere, oceans, cryosphere, and hydrosphere (Tapley et al. 2019; Chen et al. 2022). Thus, gravity field-related products contribute to several Essential Climate Variables (ECVs), which are critical indicators for assessing the Earth's changing climate, defined by the Global Climate Observing System (GCOS 2022). A prominent example is Terrestrial Water Storage (TWS, Humphrey et al. 2023), i.e., the total amount of water stored in all continental compartments, which is an ECV that can only be derived from gravity measurements.

Nowadays, dedicated gravity field missions are based on the principle of Low-Low Satellite-to-Satellite Tracking (LL-SST, Rummel et al. 2002), using ultra-precise inter-satellite ranging measurements between two co-orbiting spacecrafts. Data from the Gravity Recovery and Climate Experiment (GRACE, Tapley et al. 2004) and its successor mission GRACE-Follow-On (GRACE-FO, Landerer et al. 2020) allow to recover monthly snapshots of the Earth's gravity field in terms of global spherical harmonic (SH) coefficients with a typical maximum degree of 60 or 96 and an effective spatial resolution of about 300 km (Dahle et al. 2025).

The temporal resolution is limited by the time needed to achieve a global ground track coverage. As this takes about a month for a GRACE-like mission, derived gravity field models suffer from temporal aliasing errors (Zingerle et al. 2024), induced by sub-monthly mass transports, e.g., due to atmospheric and oceanic mass variations. To mitigate the

✉ Thomas Grombein
thomas.grombein@kit.edu

[1] Geodetic Institute, Karlsruhe Institute of Technology (KIT), Englerstr. 7, 76131 Karlsruhe, Germany

[2] Astronomical Institute, University of Bern, Sidlerstrasse 5, 3012 Bern, Switzerland

Published online: 22 September 2025

impact, short-term gravity field signals are typically reduced from the observations based on background models and dealiasing products (e.g., Dobslaw et al. 2017).

In the GRACE/-FO gravity field time series, there are several missing and degraded monthly solutions (e.g., due to instrument shutdowns or periods of near-repeat orbits) as well as a larger gap of about one year between both missions. Although the realization of the next gravity field mission GRACE-Continuity (GRACE-C, Bender et al. 2025) is underway, another substantial gap in the time series is possible, as GRACE-FO has already been affected by two major failures (Landerer et al. 2020), which could end the mission at any time.

In addition to dedicated gravity field missions, the analysis of orbital perturbations of Low Earth Orbiting (LEO) satellites allows to recover large-scale gravity field signals (spatial scales of about 800–1000 km). For this purpose, the satellite's motion needs to be tracked precisely for example by an onboard Global Navigation Satellite System (GNSS) receiver. This measurement principle, called High-Low SST (HL-SST, Rummel et al. 2002), was first realized in the CHAllenging Minisatellite Payload (CHAMP, Reigber et al. 2002) mission. Eligible LEO satellites must be equipped with (high-quality) dual-frequency GNSS receivers to achieve the required orbit accuracy of a few cm. Furthermore, the satellite's attitude data is needed to track its center of mass.

Although less sensitive, HL-SST can provide valuable gravity field information for periods where no LL-SST measurements are available. In previous studies, this approach has mainly been applied to scientific Earth observation satellites, demonstrating that it is feasible to recover both static and monthly gravity field solutions. See for example Weigelt et al. (2013), Guo et al. (2020) and Arnold et al. (2023a) for studies related to CHAMP, GRACE/-FO and the Gravity field and steady-state Ocean Circulation Explorer (GOCE, Floberghagen et al. 2011) mission, respectively. Furthermore, to bridge the gap between GRACE and GRACE-FO, gravity field information derived from GNSS data of the magnetic-field mission Swarm (Friis-Christensen et al. 2008) was employed in several studies, see, e.g., Richter et al (2021). This missions consists of three identical satellites with the lower flying pair Swarm-A and Swarm-C (altitude: ∼440 km) and the higher-flying Swarm-B (altitude: ∼510 km). To provide consolidated and improved products, monthly Swarm-based gravity field models computed by different institutes are being operationally combined (Teixeira da Encarnação et al 2020) in the framework of the International Combination Service for Time-variable Gravity Fields (COST-G, Jäggi et al. 2020).

In addition to single-mission combinations, HL-SST solutions based on data from multiple LEO satellites is important to i) further improve the spatial resolution, ii) ensure a continuous and uninterrupted time series, and iii) benefit from complementary orbital configurations. Examples of HL-SST combinations can be found in the studies of Meyer et al. (2019), Grombein et al. (2022), or Weigelt et al. (2024), where also Satellite Laser Ranging (SLR) data was incorporated to improve the very low-degree coefficients.

In addition to the growing number of scientific LEO satellites that are suitable for HL-SST, there is an even stronger increase in the amount of commercial nano-satellites (Kopacz et al. 2020). However, the huge potential of GNSS data collected by commercial mega constellations has not yet been fully exploited for gravity field recovery. On the one hand, the vast amount of data can contribute to a significant increase in the spatio-temporal resolution and thus address the problem of temporal aliasing. On the other hand, the GNSS data quality may be limited and needs to be investigated in the context of HL-SST. It should be noted that there are some simulation studies (e.g., Gunter et al. 2011; Zhou et al. 2020; Pfaffenzeller and Pail 2023) using satellite constellations and networks for gravity field determination, but a comprehensive analysis based on real data is still lacking.

Beside a restricted data availability (e.g., Liu et al. 2024), a limitation is the use of (low-cost) single-frequency GNSS receivers that do not meet the HL-SST requirements mentioned above. Here, the constellation of Spire Global Inc. is of special interest as it consists of a growing fleet of currently more than 100 nano-satellites (Cappaert 2020), which are equipped with dual-frequency GNSS receivers and an attitude determination and control system (Angling et al. 2021). These satellites have a multi-sensor payload, fly at altitudes between 400 and 650 km, and are designed for remote sensing applications with a focus on GNSS-based radio occultation and reflectometry (Jales et al. 2023). The nano-satellites used by Spire Global are standardized 3U CubeSats (Johnstone 2020) based on the in-house developed Low Earth Multi-Use Receiver (LEMUR) platform with a dimension of $10 \times 10 \times 34$ cm. The GNSS receiver is attached to a zenith-looking antenna and two side-mounted antennas for radio occultation measurements. For the purpose of Precise Orbit Determination (POD) and consequently HL-SST, the zenith-looking antenna is used, which tracks signals from the Global Positioning System (GPS).

Following an Announcement of Opportunity call from the European Space Agency (ESA), access to selected Spire data was granted to the Astronomical Institute of the University of Bern (AIUB) for the project "Precise Orbit Determination of the Spire Satellite Constellation for Geodetic, Geophysical, and Ionospheric Applications". This comprises GNSS and attitude data from nine CubeSats (eight in a sun-synchronous orbit and one in a low-inclined orbit) for a six-month period (May to Oct 2020). Based on this data, Arnold et al. (2023b) analyzed the performance and quality of GNSS data from three Spire CubeSats for POD. Compared to a scientific LEO satellite, they found increased carrier phase residuals

by a factor of 2–3 and a significantly higher noise level in the code observations, which prevented a successful ambiguity fixing (i.e., only ambiguity-float orbit solutions were derived). However, the valuable contribution of Spire data to geodetic and geophysical applications has been demonstrated, e.g., in the case of reference frame determination (Kobel et al. 2024) and ionosphere reconstruction (Schreiter et al. 2024).

In the current study, we will use the provided Spire GNSS data from all nine CubeSats to perform gravity field recovery via HL-SST. In a first step, the focus is on a comprehensive quality analysis of the derived gravity field information rather than on the feasibility of increasing the temporal resolution. Therefore, we stick to monthly gravity fields, which allows an assessment with respect to i) a superior reference (monthly GRACE-FO models) and ii) HL-SST solutions derived from a scientific satellite mission. In the latter case, we will use Swarm-B as an example due to its comparable orbital altitude during the considered time period. The derived monthly solutions consist of static gravity field coefficients with respect to a reference epoch (i.e., the middle of the data span of the respective month). As this case study is based on data from only six month, time-variable gravity field coefficients are not co-estimated. Thus, the analysis and quantification of time-variable gravity signals are beyond the scope of this study.

The paper is organized as follows: in Sect. 2 details about the Spire CubeSats data is provided and the used methods for orbit and gravity field processing are described. While Sect. 3 analyzes the quality of the derived monthly Spire-based gravity fields, Sect. 4 focuses on the benefit of combining these individual solutions. In Sect. 5, a comparison to Swarm-B gravity fields is provided and the impact of additional Spire data for a combination is assessed. Finally, Sect. 6 concludes with a summary and an outlook.

Table 1 Overview of the nine Spire CubeSats analyzed in this study

Group	Spire-FM	Satellite bus	Altitude	Inclination
G1	099	LEMUR2_3.4	~ 505 km	~ 97.5°
	101	LEMUR2_3.4		
	102	LEMUR2_3.4		
G2	103	LEMUR2_3.4	~ 530 km	~ 97.5°
	104	LEMUR2_3.4		
	106	LEMUR2_3.4		
	107	LEMUR2_3.6		
	108	LEMUR2_3.6		
G3	115	LEMUR2_3.4	~ 570 km	~ 37.0°

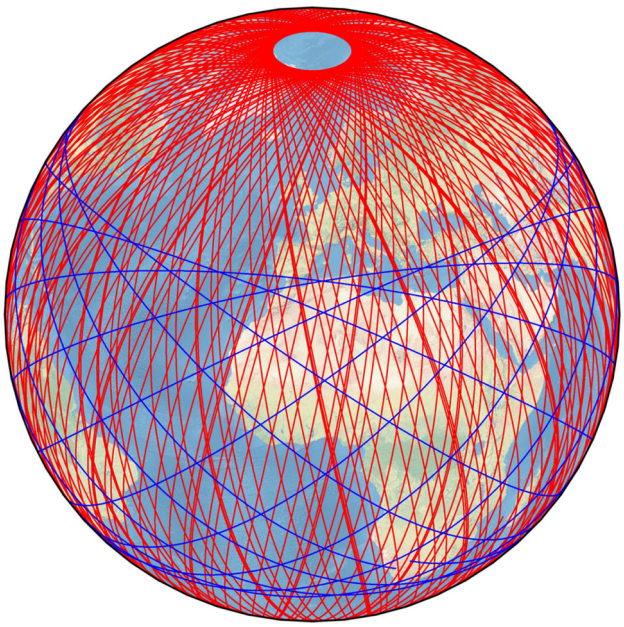

Fig. 1 Satellite ground tracks of Spire CubeSats from group G1 and G2 (red curves) and the low-inclined Spire-FM 115 (blue curve) for an exemplary day (1 May 2020); groups are defined according to Table 1

2 Data and processing

The GNSS and attitude data from nine Spire CubeSats available for this study cover the period between May and Oct 2020 (184 days) and both have a sampling rate of 1 Hz. Table 1 provides an overview of the CubeSats and classifies them into three groups according to their different orbital characteristics. The first group (G1) of CubeSats, i.e., flight model (FM) 099, FM101, FM102, has the lowest altitude of about 505 km and uses a retrograde sun-synchronous orbit with an inclination of about 97.5°. The second group (G2), consisting of five Spire CubeSats (FM103, FM104, FM106, FM107, and FM108), has nearly the same sun-synchronous orbit, but uses a slightly higher altitude of about 530 km. The last CubeSat Spire-FM115 (third group, G3) has the highest altitude of about 570 km and offers a low-inclined orbit (inclination of about 37.0°). The CubeSats were all launched in 2019 and build upon the LEMUR platform in major version 3.4 (or 3.6 in the case of FM107 and FM108).

Figure 1 visualizes the ground tracks of the Spire CubeSats involved in this study for an exemplary day (1 May 2020). The red curves represent the orbits of the CubeSats from groups G1 and G2. As a consequence of the sun-synchronous orbit, these CubeSats have a polar gap of about 7.5°, where no GNSS data is collected. Furthermore, it is notable that the daily ground tracks from eight CubeSats can already provide a homogeneous coverage. The blue curve in Fig. 1 illustrates the orbit of Spire-FM115 (G3), which provides an improved observation geometry with denser ground track coverage for regions at lower latitudes.

There are several HL-SST approaches to recover gravity field information from GNSS data of LEO satellites, see, e.g., Baur et al. (2014) for an overview. Most methods follow a two-step procedure. The first step consists of a POD, where the collected GNSS tracking data is used to derive kinematic orbit positions, i.e., three-dimensional position coordinates at discrete epochs. These positions are purely geometrically determined and independent of the LEO orbital dynamics, making them suitable for a subsequent gravity field recovery (Švehla and Rothacher 2005). In the second step, the kinematic orbit positions and their covariance information are then used as pseudo-observations in a generalized orbit problem to simultaneously solve for orbit and gravity field parameters. For both steps, we consistently use the Bernese GNSS Software (Dach et al. 2015), which applies the Celestial Mechanics Approach (CMA, Beutler et al. 2010). In the following, the used procedure for the Spire-based orbit and gravity field processing is described in more detail.

2.1 Precise orbit determination (POD)

For orbit determination, we follow the LEO POD strategy of Jäggi et al. (2006), tailored to Spire CubeSats as described in Arnold et al. (2023b). The GNSS data (i.e., code and carrier phase observations) is taken from the POD antennas using an elevation cutoff angle of 0°. In the analyzed time period, the average number of GPS satellites tracked by the Spire CubeSats ranges between 8.0 and 9.3. The attitude data are provided in terms of quaternions as described in Arnold et al. (2023b).

The code observations are used for the receiver clock synchronization with GPS time and to derive a first coarse orbit, which is the basis for an iterative phase data screening. Subsequently, the ionosphere-free linear combination is derived from the undifferenced phase observations and utilized in a Precise Point Positioning (PPP, Zumberge et al. 1997) approach. The processing is performed in daily orbital arcs by a batch least-squares adjustment. The final GNSS products (e.g., orbits, clocks, and Earth rotation parameters) from the Center of Orbit Determination in Europe (CODE, Dach et al. 2024) analysis center were considered. Although the Spire CubeSats are built identically, Arnold et al. (2023b) detected significant differences between the patterns of the receiver antenna phase center variations (PCV) for different Spire FMs. Therefore, an individual in-flight calibrated PCV map was generated for each receiver antenna onboard of the nine analyzed Spire CubeSats, following an iterative residual stacking approach (cf. Jäggi et al. 2009).

Beside kinematic orbits, the POD results also comprise reduced-dynamic orbit solutions (Jäggi and Arnold 2017). They represent the satellite's trajectory by a set of initial conditions and additional empirical parameters (Wu et al. 1991). As a particular solution of the equation of motion, these orbits strongly dependent on the assumed force models and would therefore bias a subsequent gravity field recovery. However, as reduced-dynamic orbits are more robust to outliers, they will be used as a reference for screening kinematic positions (see Sect. 2.2).

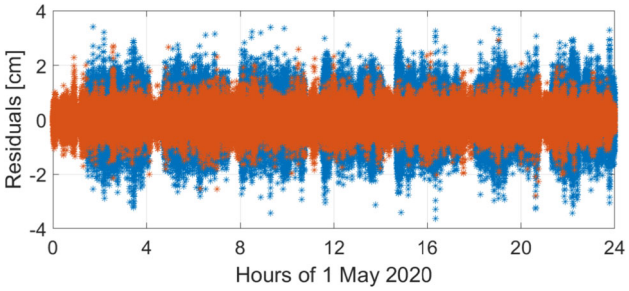

Fig. 2 Carrier phase residuals (1 s sampling) of the kinematic orbit determination for Spire-FM099 (blue) and Swarm-B (red) for an exemplary day (1 May 2020)

As also noted in Arnold et al. (2023b), the Spire receiver clock corrections estimated during the POD show relatively large drifts and regular jumps. Therefore, the epochs of the kinematic positions differ significantly from integer seconds. Similar to the experience with GOCE (Arnold et al. 2023a), it is essential to consider the fractional part of the time argument with a sufficient number of digits when Spire kinematic positions are used for gravity field determination.

To illustrate the quality of the GNSS data collected by the Spire CubeSats, Fig. 2 presents the carrier phase residuals obtained from the kinematic orbit determination, exemplarily for Spire-FM099 on 1 May 2020. For comparison, Fig. 2 also shows corresponding residuals from Swarm-B. It can be seen that the residuals for the Spire CubeSat have a significantly higher noise level. This is also reflected in the a posteriori RMS values of the residuals, where Spire-FM099 (0.82 cm) has a value about twice as large as Swarm-B (0.36 cm). This is consistent with the aforementioned factor of 2–3 reported by Arnold et al. (2023b). Another aspect that can be gathered from Fig. 2 are the frequent gaps in the Spire GNSS data. This is a consequence of GNSS receivers onboard the Spire CubeSats being switched off regularly due to power constraints between the different payloads (Cappaert et al. 2021). On average, the Spire GNSS data used in this study contain 7–10 gaps per day with a duration of 25–35min. Data from CubeSats FM107 and FM108 show significantly more gaps (24–28 per day), but of shorter duration (15–16 min).

2.2 Gravity field recovery

As a pre-processing step for gravity field recovery, the kinematic orbit positions of the Spire CubeSats are screened with respect to the corresponding reduced-dynamic orbits in order to remove outliers with a 3D-difference larger than 0.10 m (on

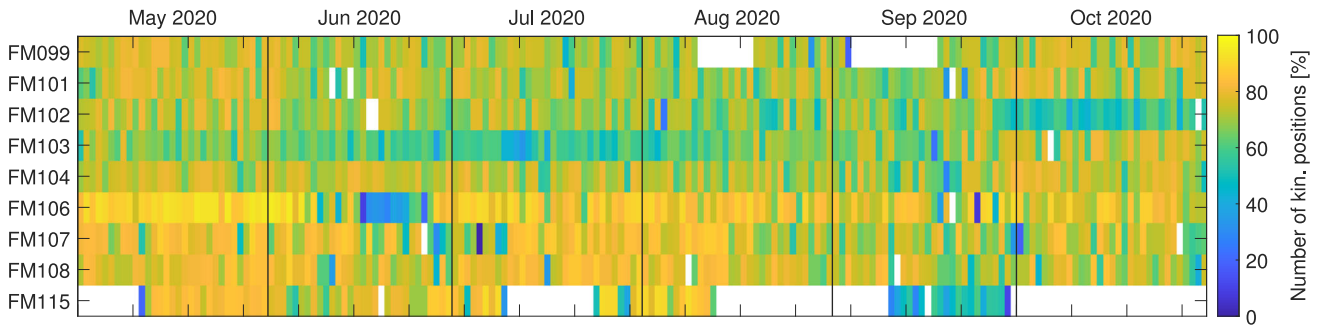

Fig. 3 Daily percentages of available screened kinematic positions (with respect to the maximum number of 86400 positions per day according to the 1 s sampling) for different Spire CubeSats in the time period between May and Oct 2020. Note that a white color indicates that no positions are available for that day

average 4.7 % of the epochs). This screening and the frequent data gaps restrict the number of epochs available for gravity field recovery. Fig. 3 specifies the resulting daily percentages of available kinematic positions for the nine Spire CubeSats in the analyzed time span. A white color indicates that data is missing for the whole day. While this is only occasionally the case for most of the CubeSats, larger time spans are missing for FM099 (23 days in Aug and Sep) and FM115 (86 days in May, Jul, Aug, Sep, and Oct). Overall, the percentages of available kinematic positions for the nine CubeSats varies between 38 % (FM115) and 78 % (FM106) with an average value of 66 %. For a few months, selected CubeSats provide only a very limited number of kinematic positions, such as FM102 in Oct, FM103 in Jul as well as FM115 in Sep. Here, it is necessary to check whether the geographical distribution of the remaining positions is sufficient to derive independent monthly gravity field solutions. On average, most kinematic positions are obtained for May (74 %), while only 60 % are available for Sep.

Based on the procedure described in Jäggi et al. (2016) and Grombein et al. (2022), gravity field recovery is accomplished as a generalized orbit determination problem. Figure 4 illustrated the processing flow, which is briefly summarized in the following. In a first step, an initial orbit determination is carried out to generate a priori orbits on a daily basis. For this purpose, the 1 s Spire kinematic positions are weighted according to their epoch-wise covariance information and are fitted over daily arcs by an iterative numerical integration based on the a priori force models specified in Table 2. For parameterization, six daily Keplerian elements are set up as well as empirical orbit parameters to absorb non-gravitational forces and to compensate for remaining model deficiencies. These additional parameters are i) daily constant accelerations in radial (R), tangential (T), and normal (N) directions, and ii) piecewise-constant RTN accelerations at 15 min intervals with 10 nm s^{-2} constraints.

In a second step, orbit and gravity field parameters are estimated simultaneously in terms of a generalized orbit improvement. To this end, the actual orbits are linearized around the computed a priori orbits and are expressed as truncated Taylor series with respect to the unknown parameters. In the case of gravity field parameters, (fully normalized) spherical harmonic (SH) coefficients $\{\overline{C}_{nm}, \overline{S}_{nm}\}$ are set up, where n and m are the SH degree and order. Based on the partial derivatives of the Taylor series, daily normal equations (NEQs) are generated.

After pre-eliminating arc-specific orbit parameters, daily NEQs are accumulated (stacked) month-wise for each CubeSat using Variance Component Estimation (VCE, Lasser 2023, Chp.3.3). This is done in an iterative way, where each daily NEQ gets a weight based on its contribution to the monthly solution. Starting with equal weights, a sufficient level of convergence is usually reached after four iterations. The final monthly NEQ is then inverted to solve for monthly SH coefficients up to degree and order (d/o) 70 without applying any regularization.

Note that the maximum degree is far above the expected sensitivity of HL-SST (cf. Sect. 1), but has been chosen to prevent an omission error from propagating into the low-degree SH coefficients (e.g., Grombein et al. 2022). For reference, Teixeira da Encarnação et al (2020) analyzed the geophysical signal content in Swarm-based solutions and found that it is confined to degrees up to 12, while higher degrees are dominated by noise.

3 Spire-based gravity field solutions

In total, 48 monthly (satellite-specific) gravity field solutions based on the kinematic positions from the Spire CubeSats of groups G1 and G2 have been computed for the considered time period (May to Oct 2020). In the case of FM115 (group G3), no individual monthly solutions can be generated due to the insufficient global coverage resulting from the low inclination of this CubeSat (see Fig. 1). All monthly solutions are independent of each other, as no temporal filtering is applied as in Zhong et al. (2021) or Weigelt et al. (2024).

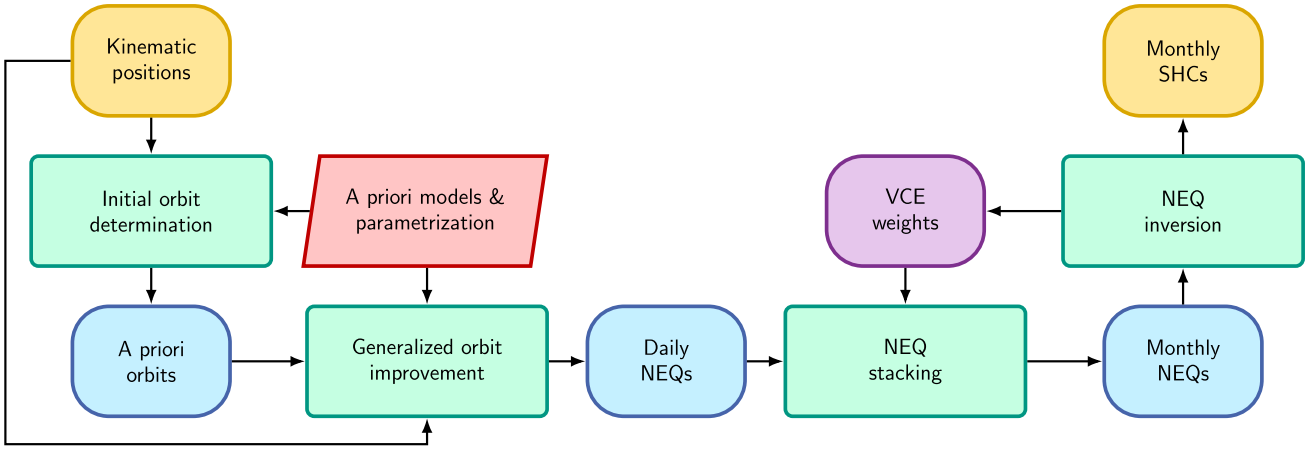

Fig. 4 Process flow for gravity field recovery with the Celestial Mechanics Approach. Abbreviations: Normal equations (NEQs), Variance Component Estimation (VCE), Spherical Harmonic Coefficients (SHCs)

Table 2 Overview of the a priori force models and their maximum degree and order (d/o) used for Spire-based gravity field recovery

Force	Model	Max. degree
A priori gravity field	AIUB-GRACE03S [a]	d/o 70 (static)
3rd body attractions	JPL DE421 [b]	–
Solid Earth	IERS2010 conv. [c]	–
Ocean tides	FES2014b [d]	d/o 100
Relativistic corrections	IERS 2010 conv. [c]	–
De-aliasing	AOD1B RL06 [e]	d/o 100
Pole tides	IERS 2010 conv. [c]	–
Atmospheric tides	AOD1B RL06 [e]	d/o 100
Ocean pole tides	Model by Desai [f]	d/o 100

[a] Jäggi et al. (2011) [b] Folkner et al. (2009) [c] Petit and Luzum (2010) [d] Lyard et al. (2021)
[e] Dobslaw et al. (2017) [f] Desai (2002)

To assess the performance of the Spire-based solutions, we use the monthly ITSG-Grace2018 models (Kvas et al. 2019) as a reference, which are based on independent and superior GRACE-FO inter-satellite ranging data. For each month and CubeSat, we then calculate the differences

$$\begin{Bmatrix} \Delta\overline{C}_{nm} \\ \Delta\overline{S}_{nm} \end{Bmatrix} = \begin{Bmatrix} \overline{C}^{\,\mathrm{Model}}_{nm} \\ \overline{S}^{\,\mathrm{Model}}_{nm} \end{Bmatrix} - \begin{Bmatrix} \overline{C}^{\,\mathrm{Ref}}_{nm} \\ \overline{S}^{\,\mathrm{Ref}}_{nm} \end{Bmatrix} \tag{1}$$

between the SH coefficients of the computed Spire solution (superscript 'Model') and the GRACE-FO reference solution (superscript 'Ref'). For analysis in the spectral domain, difference degree amplitudes (in terms of geoid heights) are computed by

$$\Delta c_n = R \left[\sum_{m=0}^{n} \left(\Delta\overline{C}^2_{nm} + \Delta\overline{S}^2_{nm} \right) \right]^{1/2}, \tag{2}$$

where R is the radius of the Earth. For comparisons in the spatial domain, the coefficient differences in Eq. (1) are synthesized to generate global geographical grids of geoid height differences

$$\Delta h\,(\varphi, \lambda) = R \sum_{n=0}^{N} \sum_{m=0}^{n} \Delta\overline{C}_{nm}\, \overline{Y}^{C}_{nm} + \Delta\overline{S}_{nm}\, \overline{Y}^{S}_{nm}, \tag{3}$$

where (φ, λ) are the latitude and longitude of a grid point, N is the maximum degree of the synthesis (here: $N = 70$), and

$$\begin{Bmatrix} \overline{Y}^{C}_{nm} \\ \overline{Y}^{S}_{nm} \end{Bmatrix} = \begin{Bmatrix} \cos m\lambda \\ \sin m\lambda \end{Bmatrix} P_{nm}\,(\sin\varphi) \tag{4}$$

are the (fully normalized) surface spherical harmonic functions that depend on the associated Legendre functions P_{nm}.

In a first step, we analyze and compare the quality of the satellite-specific solutions by taking May 2020 as an example (the month with the most available positions according to Fig. 3). For each CubeSat, Fig. 5 visualizes the geoid height differences. To focus on the relevant signal content (i.e., the long-wavelength part) and suppress the noise of the higher degrees, a Gaussian filter with a radius of 700 km is applied to the geoid height differences (cf. Wahr et al. 1998). Fig. 5

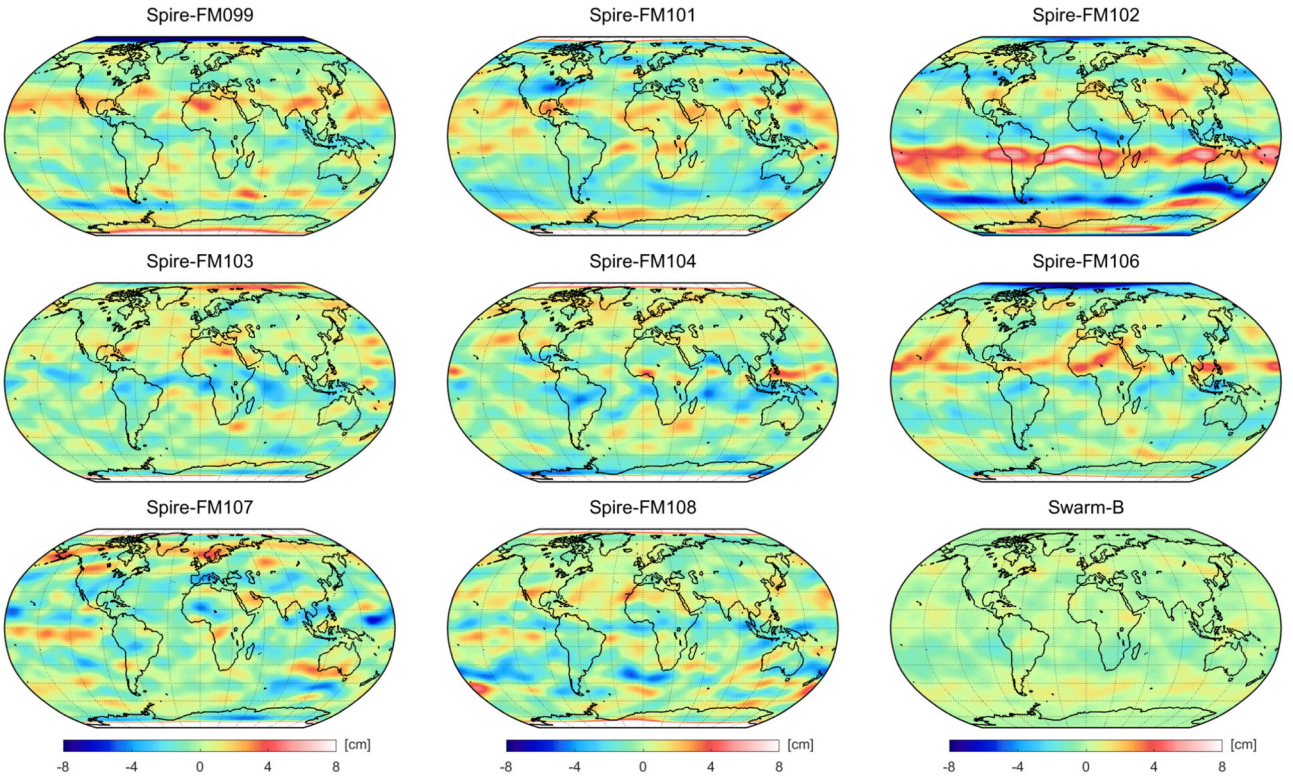

Fig. 5 Geoid height differences with respect to the monthly ITSG-Grace2018 model of Spire-based gravity field solutions for May 2020 derived from GNSS data of CubeSat FM099, FM101, FM102 (top row), FM103, FM104, FM106 (middle row), and FM107, FM108 (bottom row). For comparison, geoid height differences are also shown for a Swarm-B solution (bottom right). Gaussian smoothing with a radius of 700 km is applied

also provides results for a Swarm-B HL-SST solution that has been processed by applying the same approach as described for Spire CubeSats in Sect. 2.2.

Consistent with the findings derived from Fig. 2, geoid height differences exhibit a significantly higher noise level in the case of Spire-based solutions compared to Swarm-B, with averaged amplitudes of about ±6 cm and ±2 cm, respectively. Moreover, the geoid height differences for most of the CubeSat solutions reveal some non-geophysical signatures, particularly in terms of disturbances extending in an east–west direction along various geographical latitudes. Depending on the CubeSat, these signatures occur in a different number of bands with varying widths, amplitudes and signs.

Due to their structure along latitudes, the artifacts are related to zonal coefficients (i.e., SH coefficients with $m = 0$). For a further analysis in the spectral domain, Fig. 6 provides difference degree amplitudes for the gravity field solution of Spire-FM102, which is the most affected CubeSat according to Fig. 5. The red curve in Fig. 6 shows difference degree amplitudes based on all SH coefficients and indicates some suspiciously larger deviations for selected lower degrees, e.g., $n \in \{5, 6, 7, 8, 12, 14\}$. To analyze the contribution of zonal coefficients, difference degree amplitudes presented by the yellow curve in Fig. 6 are based solely on non-zonal SH coefficients. Comparing both curves, it becomes obvious that the zonal coefficients are mainly responsible for the discrepancies visible in the aforementioned degrees.

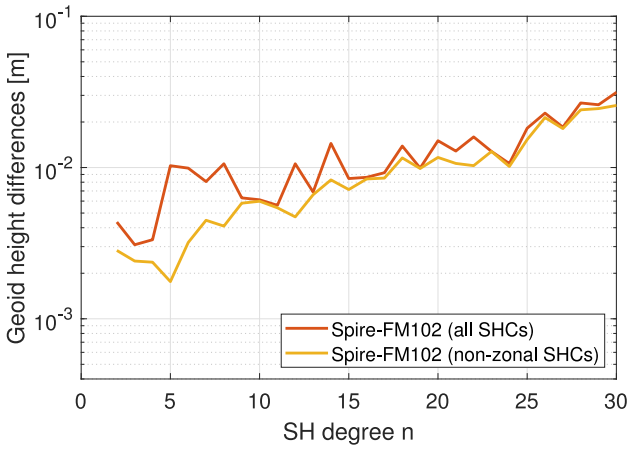

Fig. 6 Difference degree amplitudes in terms of geoid heights with respect to the monthly ITSG-Grace2018 model of Spire-based gravity field solutions for May 2020 in the case of FM102. Results are shown based on all SH coefficients (SHCs, red curve) and only non-zonal SHCs (yellow curve)

To see the impact in the spatial domain, Fig. 7 shows the geoid height differences for FM102 in the case of zonal (top left) and non-zonal (bottom left) SH coefficients. If only zonal coefficients are considered, the artifacts are prominently visible and localized in two bands along the latitudes of $-15°$ and $-50°$. On the other hand, when only non-zonal coefficients are taken into account, these signatures disappear completely, confirming that they are mainly driven by discrepancies in selected zonal coefficients. Note that the affected degrees vary slightly depending on the specific month and CubeSat (not shown).

When analyzing possible reasons for these horizontal artifacts, it was found that they are related to yaw-flip maneuvers of the Spire CubeSats. Such maneuvers are performed once per orbit to ensure a proper orientation of the solar panels in direction to the sun. In Fig. 7 (right) monthly averaged values of yaw angles (i.e., rotation around the nadir-pointing z-axis) for Spire-FM102 are visualized in terms of $1° \times 1°$ geographical bins. For descending arcs (Fig. 7, top right), instantaneous changes of the yaw angle by about 100° occur systematically at latitudes around $-15°$, matching the location of the most prominent artifact in Fig. 7 (top left). Analogously, the locations of signatures at latitudes around $-50°$ are clearly correlated with those of the yaw flips in the ascending arcs (Fig. 7, bottom right). Note that color changes between dark purple ($-180°$) and yellow (180°) do not correspond to yaw flips. The reason why yaw-flip locations map into the gravity field is not yet fully understood. It may be an indication for issues related to the uncertainties of the used phase center offset values that were provided by Spire (Arnold et al. 2023b). Correlations between yaw-flip locations and artifacts in the derived gravity fields can also be seen for other months and CubeSats (not shown). However, as will be shown in Sect. 4, these signatures can be mitigated to a large extent by combining the satellite-specific CubeSat solutions.

To quantify the quality of the individual CubeSat solutions and how it changes over the analyzed six-month period, Table 3 provides area-weighted root mean square (RMS) values of geoid height differences for all CubeSat solutions. These RMS values refer to the region with latitudes $|\varphi| < 80°$ to avoid being affected by the CubeSat's polar gap (see large differences for areas near the North and South poles in Fig. 5). According to the RMS values specified in Table 3, the monthly satellite-specific gravity field solutions have a comparable quality level over the considered time period. For more than 80 % of the derived solutions, the RMS values are between 1.0 and 1.5 cm, indicating no systematically different behavior for CubeSats of group G1 and G2. Most of the larger RMS values can be attributed to the solutions of FM102, where the monthly variability is also considerably higher compared to the other CubeSats. In Oct 2020, the solution for FM102 suffers from large data gaps (see Fig. 3),

Table 3 Area-weighted RMS values (in cm) of geoid height differences with respect to monthly ITSG-Grace2018 models of Spire-based gravity field solutions in the period May–Oct 2020

FM	099	101	102	103	104	106	107	108
May	1.04	1.25	1.91	1.06	1.16	1.13	1.25	1.23
Jun	1.24	1.33	1.72	1.28	1.24	1.15	1.47	1.32
Jul	1.11	1.34	1.80	1.38	1.15	1.11	1.29	1.38
Aug	1.22	1.08	1.59	1.11	1.08	1.16	1.18	1.47
Sep	1.22	1.17	1.04	1.54	1.36	1.09	1.40	1.64
Oct	1.39	1.21	4.01	1.18	1.05	1.15	1.14	1.57

Note that Gaussian smoothing with a 700 km radius is applied and that all RMS values refer to the region with latitudes $|\varphi| < 80°$ in order not to be affected by the polar gap

resulting in a substantially larger RMS value of about 4 cm. Although this monthly solution is only of limited use, it could still contribute to a combination (see Sect. 4). Remarkably, the solutions for FM099 in Aug and Sep (both with an RMS value of 1.22 cm) do not appear to be significantly impaired, even though kinematic positions are not available for nine and 14 days in these months, respectively (cf. Fig. 3). On average, the best performance (1.13 cm) and most consistent quality level is achieved by the gravity field solutions derived from Spire-FM106, which is also the CubeSat that offers the largest number of kinematic positions (cf. Fig. 3). Comparing the RMS values that are averaged month-wise, gravity field solutions for Aug 2020 provide the lowest values, while the highest values are obtained for Oct 2020.

For an analysis in the frequency domain, Fig. 8 presents difference degree amplitudes for the CubeSat solutions in May 2020. In contrast to Fig. 6, the rule of thumb of van Gelderen and Koop (1997) is applied to avoid that degree amplitudes are influenced by the polar gap. Thus, depending on the degree n, the zonal and near-zonal SH coefficients with orders

$$m < \left|90° - I\right| \cdot \pi/180° \cdot n \tag{5}$$

are excluded, where I is the orbital inclination (i.e., 97.5° for the Spire CubeSats of group G1 and G2, see Table 1). Moreover, difference degree amplitudes are shown up to SH degree 70, i.e., the maximum degree of the estimated gravity fields. In this context, it should be noted again that i) the geophysical signal content of HL-SST solutions is restricted to lower degrees, and that ii) coefficients above degree 15 mainly reflect the noise of the solution.

In the left panel of Fig. 8, difference degree amplitudes are shown for the CubeSat solutions belonging to group G1. The CubeSat solutions differ mainly in the relevant lower degrees, where the quality can generally be ranked as follows: FM099 (red curve) provides the lowest difference degree amplitudes, followed by FM101 (yellow curve). Consistent with the RMS

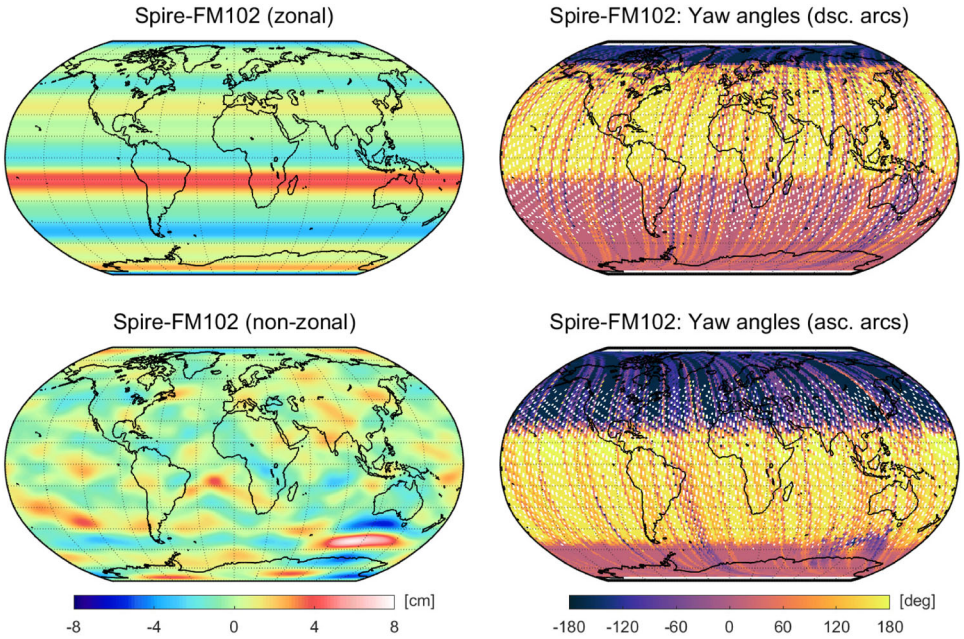

Fig. 7 Left panel: geoid height differences with respect to the monthly ITSG-Grace2018 model of Spire-based gravity field solutions for May 2020 derived from GNSS data of CubeSat FM102 showing the contribution of zonal (top) and non-zonal (bottom) SH coefficients. Right panel: Monthly averaged values of yaw angles for Spire-FM102 in terms of $1° \times 1°$ geographical bins in the case of descending (top) and ascending (bottom) arcs

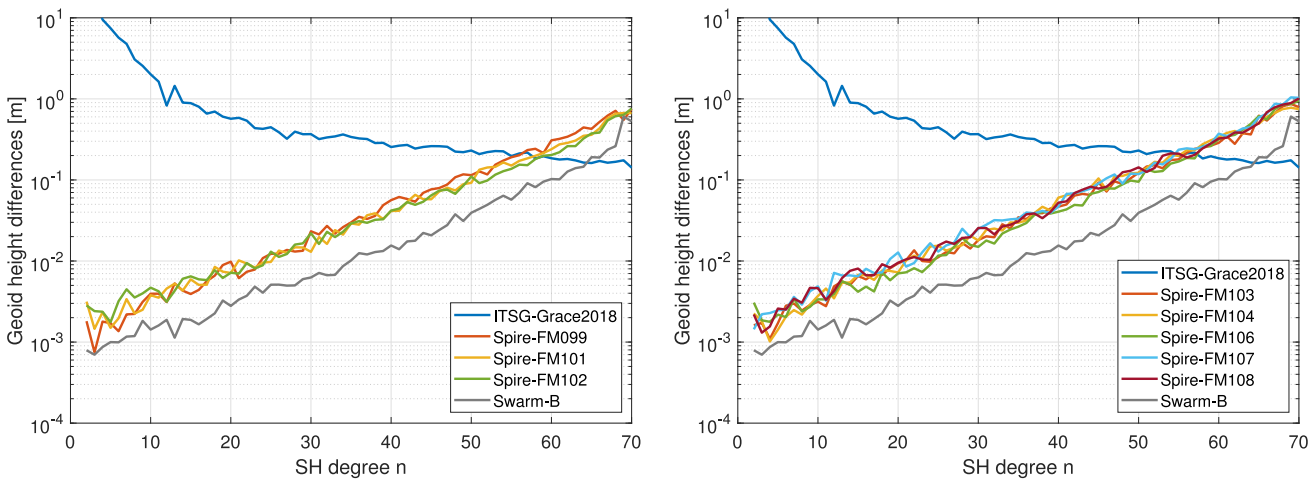

Fig. 8 Difference degree amplitudes in terms of geoid heights with respect to the monthly ITSG-Grace2018 model (blue curve) of Spire-based gravity field solutions for May 2020. Left panel: CubeSat solutions from group G1, i.e., FM099 (red curve), FM101 (yellow curve), and FM102 (green curve). Right panel: CubeSat solutions from group G2, i.e., FM103 (red curve), FM104 (yellow curve), FM106 (green curve), FM107 (light blue curve), and FM108 (dark red curve). For comparison, difference degree amplitudes are also shown for a solution based on GNSS data from Swarm-B (gray curve). Zonal and near-zonal coefficients are excluded according to van Gelderen and Koop (1997)

values in Table 3, the gravity field recovery obtained from the FM102 data (green curve) exhibit the largest deviations from the monthly ITSG-Grace2018 reference model. Note that this order is reversed to some extent in the case of higher degrees. Figure 8 also includes results for the Swarm-B solution (gray curve). The comparison reveals a quite significant difference in the quality level of the Spire and Swarm-based solutions, where the superior performance of Swarm-B can be seen throughout the spectrum. The gap between the curves can mainly be explained by the different observation noise in the GNSS data. For example, in the case of FM099 and Swarm-B, the difference corresponds to a factor of about 3, which is consistent with the comparison of the carrier phase residuals of both satellites in Sect. 2.1.

In Fig. 8 (right), difference degree amplitudes are displayed for the CubeSat solutions of group G2. The differences of these solutions to the monthly ITSG-Grace2018 model are generally in the same order of magnitude. As the CubeSats of group G2 have a higher orbital altitude, the high-frequency noise is slightly increased in these solutions compared to those of group G1. Overall, the performance of the FM106 solution (green curve) is the best over most of the

spectrum. However, for the lowest degrees, this solution is outperformed by those of FM103 and FM104 (red and yellow curves). The difference degree amplitudes for FM107 and FM108 (light blue and purple curves) are systematically larger compared to the other solutions. Again, the superior performance of the Swarm-B solution (gray curve) can be observed over the whole spectrum. This leads to the conclusion that a single Spire CubeSat gravity field solution cannot compete with the ones obtained from the dual-frequency GNSS data of a typical scientific LEO mission.

4 Combined CubeSat solutions

To improve the quality of the Spire-based gravity field information, the satellite-specific CubeSat solutions are combined on a monthly basis at NEQ-level using VCE. In the following, the performance of different combinations is examined to analyze the benefit gained from accumulating data of multiple CubeSats. According to the groups defined in Table 1, combinations are generated based on the data from three (group G1), five (group G2), eight (group G1+2), and nine (group G1+2+3) CubeSats.

Again using May 2020 as an example, Fig. 9 shows geoid height differences in the spatial domain. Focusing on the combination based on the three lower flying CubeSats of group G1 (FM099, FM101, and FM102), the geoid height differences in Fig. 9 (top left) reveal that this solution is still affected by the signatures discussed in the previous Sect. 3. Artifacts in east–west direction at latitudes around 30°, −15°, and −50°, which are also visible in the satellite-specific CubeSat solutions for FM099 and FM102 in Fig. 5, map into the combination. However, with an RMS value of 1.00 cm, the geoid height differences of the combination at least outperform all three contributing solutions (cf. Table 3). In the case of group G2 (five CubeSats), the benefit of combination becomes more significant. Prominent signatures visible in the solutions of FM106 and FM107 (cf. Fig. 5) are strongly attenuated in the combination (Fig. 9, top right), resulting in a 33 % reduced RMS value compared to the best individual contribution (FM103).

By combining the eight CubeSat solutions from groups G1 and G2, the geoid height differences with respect to the monthly ITSG-Grace2018 model can be further improved (Fig. 9, bottom left). In particular, artifacts that were still visible in the G1 combination are reduced to a large extent. However, still some systematic effects can be recognized, e.g., larger differences in the region between South America and Africa, which can be attributed to the FM102 solution (cf. Fig. 5). Finally, the 9 CubeSats combination also takes into account data from the low-inclined Spire-FM115, which can contribute to the region with latitudes $|\varphi| < 37°$. The amplitudes of the remaining anomalies in this area are considerably mitigated in the geoid height differences (Fig. 9, bottom right). The improvements gained from just one additional low-inclined CubeSat are remarkable, especially when considering that only about 50 % of the observations are available from FM115 (cf. Fig. 3). Taking the best individual solution as reference (FM099), the RMS value of the geoid height differences in May can be reduced by 4 %, 32 %, 43 % and 61 % in the case of the combinations G1, G2, G1+G2, and G1+G2+G3, respectively.

In Fig. 10, difference degree amplitudes for May 2020 are plotted, supporting the previous findings. The 3 and 5 CubeSats combinations (yellow and green curves in Fig. 10, left) provide a comparable quality over most of the spectrum. In the lower degrees, the 5 CubeSats solution has a slightly better performance, particularly in the case of degree 4. The combination consisting of group G1 and G2 (i.e., the 8 CubeSats solution, yellow curve in Fig. 10, right) reveals significant improvements across the spectrum. The impact of the low-inclined CubeSat FM115, which contributes to the 9 CubeSats solution (green curve in Fig. 10, right), is also impressively visible in the frequency domain. Most striking are the reduced amplitudes for the frequency band between degrees 5 and 15 as well as around degree 20.

In general, the level of improvement achieved by the combinations (as visible in Fig. 10) approximately follows the expected rule that N times more contributing satellites reduce the error by a factor of $\sqrt{N}$. Note that this factor can vary depending on the number of observations per CubeSat. For example, the gap between the difference degree amplitudes of the solutions based on data from one versus nine CubeSats corresponds to a factor of about $\sqrt{9} = 3$.

Figure 11 provides RMS values of geoid height differences for the whole time period and confirms that May 2020 is a representative example. In general, the more CubeSat solutions are accumulated, the smaller the monthly geoid height differences become. The only exception is Sep 2020, where the 3 CubeSats solution (G1) outperforms the 5 CubeSats solution (G2). As there is no data available from FM115 for Oct 2020, the 8 and 9 CubeSats solutions are identical. In all other months, there is a significant impact of FM115 visible, which could be expected to be even stronger when more data were usable.

To see in more detail which SH coefficients actually benefit from the contribution of the CubeSat FM115, Fig. 12 shows the standard deviations (formal errors) of the coefficients corresponding to the 8 and 9 CubeSats combinations in terms of coefficient triangles for May 2020. The 8 CubeSats solution (Fig. 12, left) provides an almost uniform error spectrum, which is consistent with the satellite-specific CubeSat solutions of group G1 and G2 (not shown). In contrast, the pattern changes considerably in the case of the 9 CubeSats solution (Fig. 12, middle). As can be seen from the percentage improvements (Fig. 12, right), the inclusion of the low-inclined CubeSat FM115 primarily provides addi-

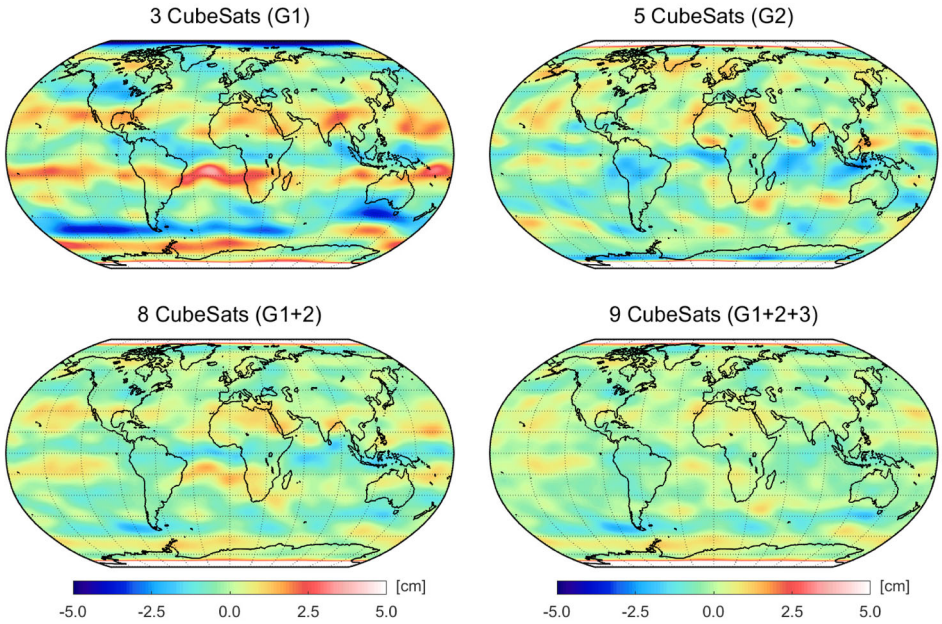

Fig. 9 Geoid height differences with respect to the monthly ITSG-Grace2018 model of combined Spire-based gravity field solutions for May 2020. Results are shown based on GNSS data from an increasing number of contributing CubeSats, i.e., three (group G1, top left), five (group G2, top right), eight (group G1+2, bottom left) and nine (group G1+2+3, bottom right); groups are defined according to Table 1. Gaussian smoothing with a radius of 700 km is applied. Note the different scaling of the color bar compared to Fig. 5

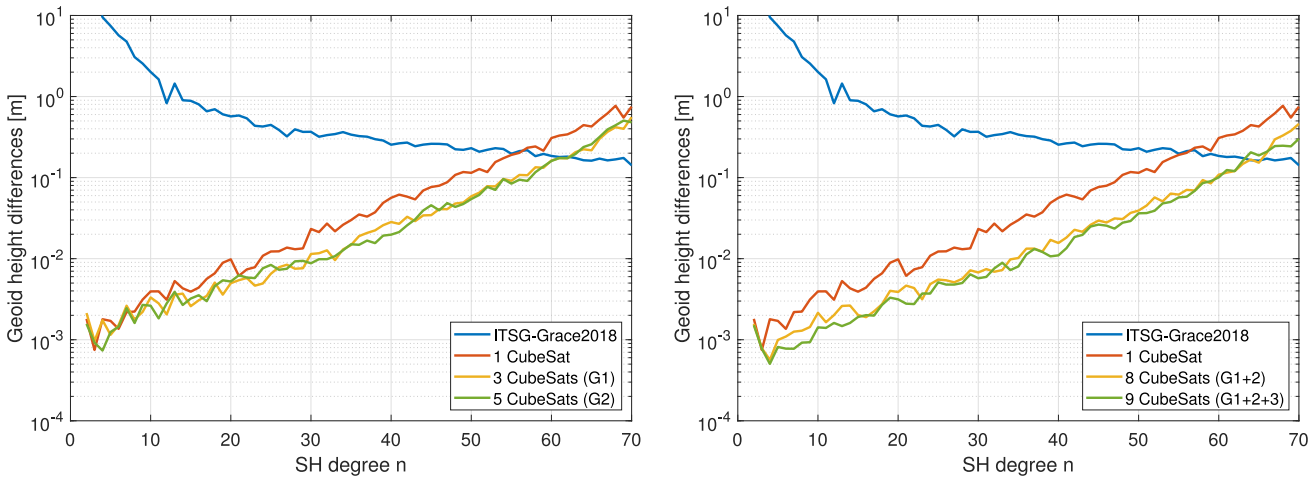

Fig. 10 Difference degree amplitudes in terms of geoid heights with respect to the monthly ITSG-Grace2018 model (blue curve) of combined Spire-based gravity field solutions for May 2020. Results are shown based on GNSS data from an increasing number of contributing CubeSats. Left panel: three (group G1, yellow curve) and five (group G2, green curve) CubeSats. Right panel: eight (group G1+2, yellow curve) and nine (group G1+2+3, green curve) CubeSats; groups are defined according to Table 1. For comparison, difference degree amplitudes are also shown for a single Spire CubeSat solution (FM099, red curve). Zonal and near-zonal coefficients are excluded according to van Gelderen and Koop (1997)

tional sensitivity for tesseral coefficients (on average about 40 % improvement with a maximum of about 50 % for orders around 25). The impact on sectorial coefficients is limited and confined to lower degrees, i.e., an averaged improvement of about 5 % for degrees with $n < 10$ and smaller than 2 % for higher degrees. For both combinations, increased standard deviations are visible for zonal coefficients, caused by the polar gap of the Spire CubeSats. However, these coefficients can still be improved by about 20 % on average. Note that the specified improvements are also representative for other months in which CubeSat FM115 contributes.

5 Comparison and combination with Swarm

For May 2020, the difference degree amplitudes shown in Fig. 13 (left) reveal a comparable performance of the 9 CubeSats combination (yellow curve) and the Swarm-B solution (green curve). This illustrates that the increased number of observations can effectively counteract the amplified observation noise that impairs the quality of a single CubeSat solution (e.g., FM099, red curve). For the lowest degrees with $n < 10$, the combined Spire solution even provides a

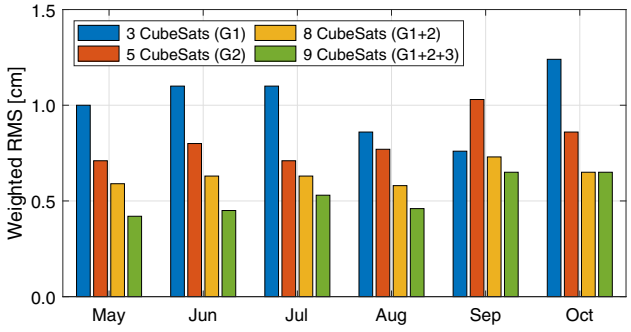

Fig. 11 Area-weighted RMS values of geoid height differences with respect to monthly ITSG-Grace2018 models of combined CubeSat solutions in the period May–Oct 2020. Note that Gaussian smoothing with a 700 km radius is applied and that all RMS values refer to the region with latitudes $|\varphi| < 80°$ in order not to be affected by the polar gap

slightly better agreement with the monthly ITSG-Grace2018 model than Swarm-B (the same holds for Jun 2020).

To study whether the Spire data can contribute to improve a Swarm gravity field, we combine the 9 CubeSats solutions with the corresponding Swarm-B solutions on a monthly basis (combination at NEQ-level). In terms of difference degree amplitudes, Fig. 13 (right) confirms that the Swarm-B-Spire combination (yellow curve) outperforms the Swarm-B-only solution (red curve) in almost all frequencies. This improvement is also reflected in the corresponding geoid height differences as shown in Fig. 14. In the case of Swarm-B (top), some larger (positive) discrepancies with respect to the monthly ITSG-Grace2018 model can be detected for latitudes around ±50°, while some negative values are concentrated along the latitude of −15°. Most of these

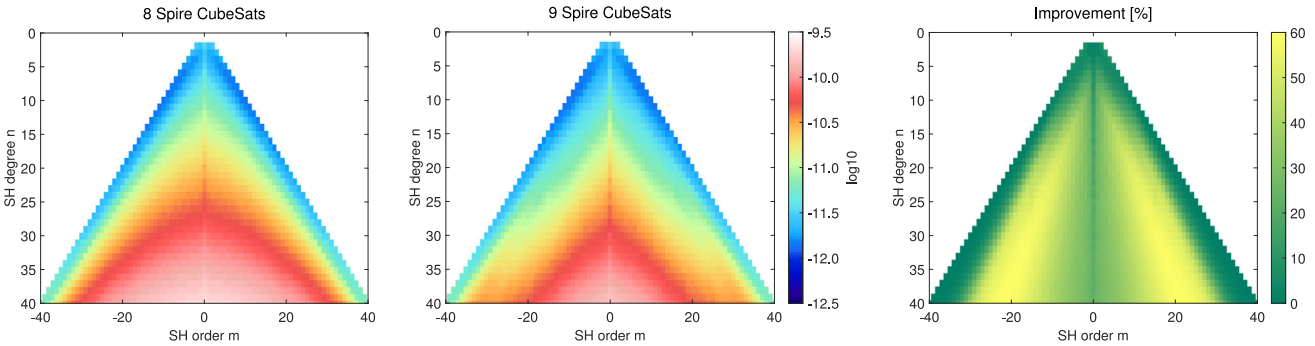

Fig. 12 Standard deviations (formal errors) of SH coefficients derived from the Spire-based gravity fields for May 2020. Results are shown for combinations based on data from eight CubeSats (G1+G2, left) and nine CubeSats (G1+G2+G3, middle). The right panel shows the percentage improvements in the standard deviations due to the inclusion of the low-inclined CubeSat FM115

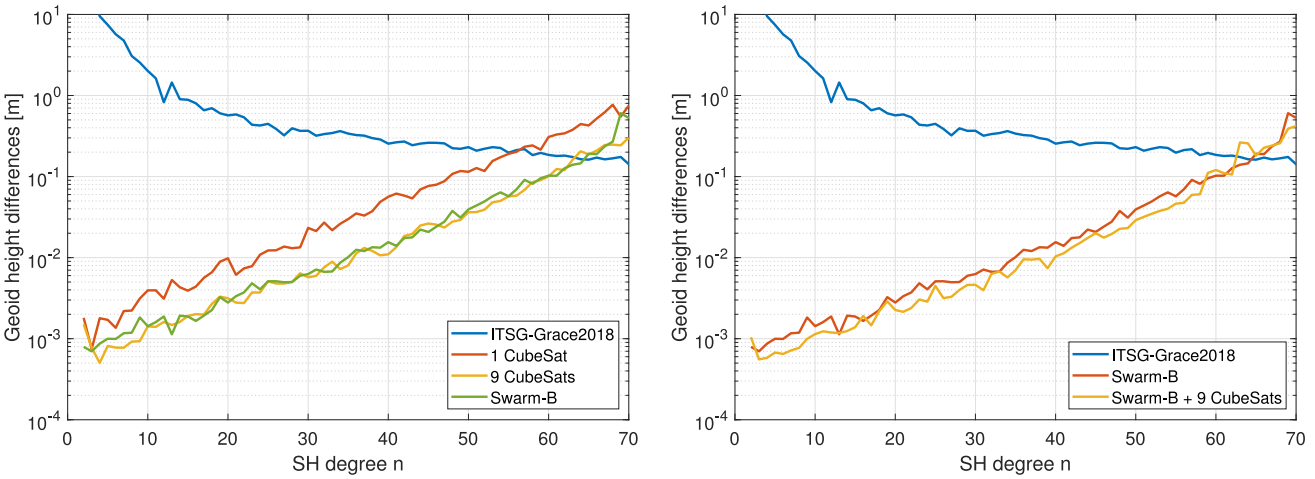

Fig. 13 Difference degree amplitudes in terms of geoid heights with respect to the monthly ITSG-Grace2018 model (blue curve) of GNSS-based gravity field solutions for May 2020. Left panel: Spire solutions based on data from a single CubeSat (FM099, red curve) and nine CubeSats (G1+G2+G3, yellow curve) as well as a Swarm-B solution (green curve). Right panel: Swarm-B (red curve) and a combination of Swarm-B and the 9 Spire CubeSats solution (G1+G2+G3, yellow curve). Zonal and near-zonal coefficients are excluded according to van Gelderen and Koop (1997)

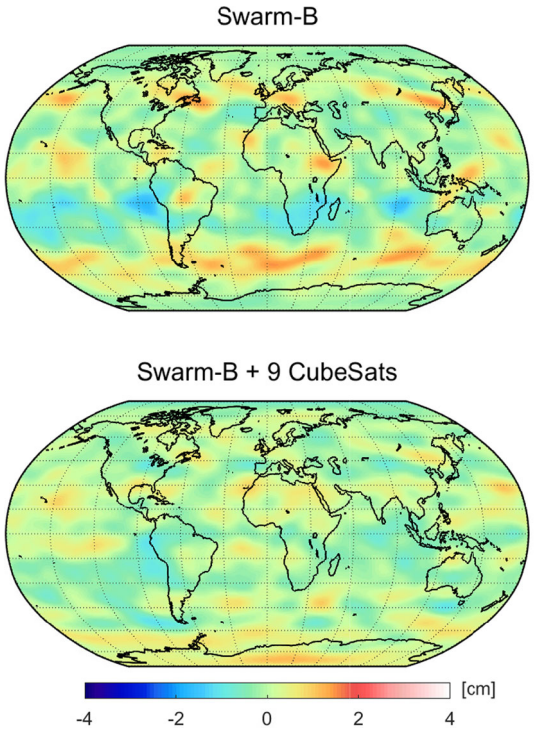

Fig. 14 Geoid height differences with respect to the monthly ITSG-Grace2018 model of GNSS-based gravity field solutions for May 2020. Results are shown for Swarm-B (top) and a combination of Swarm-B and the 9 Spire CubeSat solution (G1+G2+G3, bottom). Gaussian smoothing with a 700 km radius is applied. Note the different scaling of the color bar compared to Figs. 5 and 10

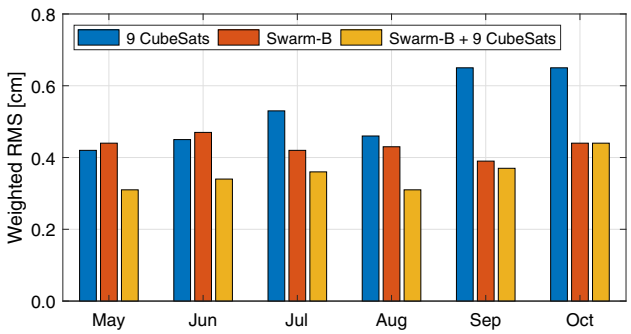

Fig. 15 Area-weighted RMS values of geoid height differences with respect to monthly ITSG-Grace2018 models of 9 CubeSat solutions (blue bars), Swarm-B solutions (red bars) and Swarm-B-Spire combinations (yellow bars) in the period May–Oct 2020. Note that Gaussian smoothing with a 700 km radius is applied and that all RMS values refer to the region with latitudes $|\varphi| < 80°$ in order not to be affected by the polar gap

anomalies are strongly mitigated in the Swarm-B-Spire combination (bottom of Fig. 14).

For quantification, Fig. 15 specifies RMS values of geoid height differences for each month (May–Oct 2020). In contrast to the monthly variability in the case of the 9 CubeSats solutions (blue bars), the RMS values for the Swarm-B solutions (red bars) reflect a more consistent quality level with only slight fluctuations. In general, the Swarm-B solutions exhibit smaller RMS values than the 9 CubeSats solutions with the exception of May and Jun 2020. In almost all months, the RMS value of the Swarm-B solution can be significantly reduced by a combination with the Spire data (yellow bars). The largest RMS improvement of about 30 % can be reached for May, Jun, and Aug 2020. Consistently, these three months also provide the smallest RMS values in the Spire time series. In the case of Jul and Sep 2020, the RMS improvement is about 15 % and 5 %, respectively. For Oct 2020, the Swarm-B solution cannot profit significantly from the additional Spire data. This can be explained by the limited data availability for this month (see Fig. 3) and in particular the missing contribution of FM115.

6 Summary and outlook

In this paper, we demonstrated that it is feasible to derive monthly gravity field solutions from GNSS data collected by nano-satellites of commercial mega constellations. For this purpose, we adopted the principle of High-Low Satellite-to-Satellite-Tracking (HL-SST), which so far has mainly been applied to scientific Low Earth orbiting (LEO) satellites. For our analysis, we used GNSS data from the Spire Global constellation, which consists of more than 100 CubeSats and provides a unique opportunity as all satellites are equipped with dual-frequency GNSS receivers. The present case study was conducted by examining data from nine Spire CubeSats covering a six-month period between May and Oct 2020. The obtained GNSS observations are first used to derive 1 s kinematic orbit positions, which are then subsequently utilized as pseudo-observations for gravity field recovery. Both steps were performed with the Bernese GNSS Software, which applies the Celestial Mechanics Approach.

In the kinematic orbit determination, the Spire GNSS observations were found to have an increased noise level, approximately 2–3 times higher than that of Swarm-B, which served as an example of a typical scientific LEO satellite at a comparable orbital altitude. The amplified observation noise directly affects the quality of the retrieved monthly gravity field solutions. This is clearly reflected in the frequency domain by evaluating difference degree amplitudes with respect to superior GRACE-FO models. Across the spectrum, there is a significant gap between the performance of the Spire CubeSat and Swarm-B solutions visible, which can also be quantified by a factor of 2–3. Moreover, most CubeSat solutions suffer from discrepancies in selected zonal spherical harmonic (SH) coefficients. In the spatial domain, this results in artifacts in east–west direction that occur at various latitudes. This was found to be correlated with yaw-flip maneuvers that are frequently performed by the CubeSats.

Overall, it can be concluded that a single CubeSat solution cannot compete with the gravity field information obtained from GNSS data of a scientific LEO satellite like Swam-B. However, it has been proven that the accumulation of CubeSat solutions (at normal equation level) can gradually improve the quality and also mitigate the aforementioned artifacts.

A combination based on data from all nine CubeSats achieves a comparable performance to Swarm-B, revealing an even higher consistency with GRACE-FO models for the lowest degrees in May and Jun 2020. For the combination, the low-inclined Spire-FM115 (inclination of 37°) provides a valuable contribution. In particular, tesseral coefficients within the frequency band between degrees 5 and 15 and around 20 benefit from the data of FM115. Furthermore, the higher spatial sampling of kinematic positions at lower latitudes enables an almost complete removal of remaining artifacts in these regions. The improvements achieved by FM115 are also remarkable, when considering that only 38 % of the data is available in the analyzed time period. We also investigated if a Swarm-B gravity field model can profit from additional Spire CubeSats data. The combination of Swarm-B and the 9 CubeSats solutions provides a significant improvement in the frequency domain (reduced difference degree amplitudes over most of the spectrum) and in the spatial domain (reduced geoid height differences with an average RMS improvement of about 20 % and maximum values of about 30 % for May, Jun, and Aug 2020).

In summary, our study has highlighted the potential and limitations of using GNSS data from commercial nanosatellites for HL-SST. Although the derived gravity field information might be less sensitive, the vast amount of observations available from mega constellations can compensate for this. This was demonstrated in this case study, where gravity field models based on GNSS data from Swarm-B could be partially outperformed by the combined contribution of nine Spire CubeSats that provide data with an increased observation noise. This raises the question of what can be expected from the possible integration of hundreds of additional CubeSats into a Multi-HL-SST time series.

As a next step, we aim to process and combine Spire data from additional CubeSats. The enhanced spatio-temporal coverage will offer the opportunity to increase the temporal resolution, i.e., to strive for sub-monthly gravity field solutions. Such information will help to reduce temporal aliasing errors of current GRACE-FO models, potentially eliminating the need for de-aliasing products. Following the promising results with Spire-FM115, the inclusion of additional low-inclined CubeSats would be desirable. Additionally, we also intend to process longer time spans (at least one year), which will allow us to estimate and study static and time-variable gravity field signals. To further improve the performance of the used gravity field recovery, the implementation of an enhanced noise modeling approach will be beneficial, such as frequency-dependent data weighting proposed by Ditmar et al. (2007).

Acknowledgements We acknowledge the support from Spire Global and the provision of Spire data by the European Space Agency (ESA) in the frame of an Announcement of Opportunity call (project No. 66978). This research was partly funded by the European Research Council under the grant agreement No. 817919 (project SPACE TIE). All views expressed are those of the authors and not of the European Research Council. Calculations for this study were performed on UBELIX, the HPC cluster at the University of Bern (https://www.id.unibe.ch/hpc). Finally, the authors would like acknowledge three anonymous reviewers as well as the associate editor for their valuable comments, which helped to improve the manuscript.

Author Contributions TG performed the gravity field processing, designed and analyzed the experiments and wrote the manuscript. DA conducted the precise orbit determination and provided kinematic orbits for Spire and Swarm. ML contributed to the software implementation for gravity field recovery and supported the processing. AJ acquired the funding and provided advice. All authors discussed the results and reviewed the manuscript.

Funding Open Access funding enabled and organized by Projekt DEAL.

Data availability Access to Spire data was granted by ESA in the frame of an Announcement of Opportunity project. The used Swarm orbits are available from Arnold and Jäggi (2021).

Declarations

Conflict of interest The authors declare no conflict of interest.

Open Access This article is licensed under a Creative Commons Attribution 4.0 International License, which permits use, sharing, adaptation, distribution and reproduction in any medium or format, as long as you give appropriate credit to the original author(s) and the source, provide a link to the Creative Commons licence, and indicate if changes were made. The images or other third party material in this article are included in the article's Creative Commons licence, unless indicated otherwise in a credit line to the material. If material is not included in the article's Creative Commons licence and your intended use is not permitted by statutory regulation or exceeds the permitted use, you will need to obtain permission directly from the copyright holder. To view a copy of this licence, visit http://creativecommons.org/licenses/by/4.0/.

References

Angling MJ, Nogués-Correig O, Nguyen V, Vetra-Carvalho S, Bocquet FX, Nordstrom K, Melville SE, Savastano G, Mohanty S, Masters D (2021) Sensing the ionosphere with the Spire radio occultation constellation. J Space Weather Space Clim 11:56. https://doi.org/10.1051/swsc/2021040

Arnold D, Jäggi A (2021) AIUB Swarm kinematic orbits, release 03. https://doi.org/10.48350/158373, Astronomical Institute, University of Bern, http://www.aiub.unibe.ch/download/LEO_ORBITS

Arnold D, Grombein T, Schreiter L, Sterken V, Jäggi A (2023) Reprocessed precise science orbits and gravity field recovery for the

entire GOCE mission. J Geod 97:67. https://doi.org/10.1007/s00190-023-01752-y
Arnold D, Peter H, Mao X, Miller A, Jäggi A (2023) Precise orbit determination of Spire nano satellites. Adv Space Res 72(11):5030–5046. https://doi.org/10.1016/j.asr.2023.10.012
Baur O, Bock H, Höck E, Jäggi A, Krauss S, Mayer-Gürr T, Reubelt T, Siemes C, Zehentner N (2014) Comparison of GOCE-GPS gravity fields derived by different approaches. J Geod 88(10):959–973. https://doi.org/10.1007/s00190-014-0736-6
Bender PL, Conklin JW, Wiese DN (2025) Short-period mass variations and the next generation gravity mission. J Geophys Res Solid Earth 130(1):e2024JB030290. https://doi.org/10.1029/2024JB030290
Beutler G, Jäggi A, Mervart L, Meyer U (2010) The celestial mechanics approach: theoretical foundations. J Geod 84(10):605–624. https://doi.org/10.1007/s00190-010-0401-7
Cappaert J (2020) The Spire small satellite network. In: Pelton JN (ed) Handbook of small satellites: technology, design, manufacture, applications, economics and regulation. Springer International Publishing, pp 1–21, https://doi.org/10.1007/978-3-030-20707-6_93-1
Cappaert J, Foston F, Heras PS, King B, Pascucci N, Reilly J, Brown C, Pitzo J, Tallhamn M (2021) Constellation modelling, performance prediction and operations management for the Spire constellation. In: Proceedings of the AIAA/USU Conference on Small Satellites, SSC21-I-13, https://digitalcommons.usu.edu/smallsat/2021/all2021/136/
Chen J, Cazenave A, Dahle C, Llovel W, Panet I, Pfeffer J, Moreira L (2022) Applications and challenges of GRACE and GRACE Follow-On satellite gravimetry. Surv Geophys 43(1):305–345. https://doi.org/10.1007/s10712-021-09685-x
Dach R, Lutz S, Walser P, Fridez P (eds) (2015) Bernese GNSS Software Version 5.2, Documentation. University of Bern, Bern, Switzerland, https://doi.org/10.7892/boris.72297
Dach R, Schaer S, Arnold D, Brockmann E, Kalarus M, Meyer U, Prange L, Stebler P, Jäggi A, Villiger A, Ineichen D, Lutz S, Willi D, Thaller D, Klemm L, Rülke A, Söhne W, Bouman J, Hugentobler U, Duan B (2024) Center of Orbit Determination in Europe (CODE) Analysis center – Technical Report 2023. In: Dach R, Brockmann E (eds) International GNSS Service Technical Report 2023 (IGS Annual Report), IGS Central Bureau and University of Bern, Bern Open Publishing, pp 49–66, https://doi.org/10.48350/191991
Dahle C, Boergens E, Sasgen I, Döhne T, Reißland S, Dobslaw H, Klemann V, Murböck M, König R, Dill R, Sips M, Sylla U, Groh A, Horwath M, Flechtner F (2025) GravIS: mass anomaly products from satellite gravimetry. Earth Syst Sci Data 17(2):611–631. https://doi.org/10.5194/essd-17-611-2025
Desai SD (2002) Observing the pole tide with satellite altimetry. J Geophys Res Oceans 107(C11):3186. https://doi.org/10.1029/2001JC001224
Ditmar P, Klees R, Liu X (2007) Frequency-dependent data weighting in global gravity field modeling from satellite data contaminated by non-stationary noise. J Geod 81(1):81–96. https://doi.org/10.1007/s00190-006-0074-4
Dobslaw H, Bergmann-Wolf I, Dill R, Poropat L, Thomas M, Dahle C, Esselborn S, König R, Flechtner F (2017) A new high-resolution model of non-tidal atmosphere and ocean mass variability for de-aliasing of satellite gravity observations: AOD1B RL06. Geophys J Int 211(1):263–269. https://doi.org/10.1093/gji/ggx302
Floberghagen R, Fehringer M, Lamarre D, Muzi D, Frommknecht B, Steiger C, Piñeiro J, da Costa, (2011) Mission design, operation and exploitation of the Gravity field and steady-state Ocean Circulation Explorer mission. J Geod 85(11):749–758. https://doi.org/10.1007/s00190-011-0498-3
Folkner WM, Williams JG, Boggs DH (2009) The planetary and lunar ephemeris DE 421. Interplanetary Network (IPN) Progress Report 42–178, NASA Jet Propulsion Laboratory, https://ipnpr.jpl.nasa.gov/progress_report/42-178/178C.pdf
Friis-Christensen E, Lühr H, Knudsen D, Haagmans R (2008) Swarm – an Earth observation mission investigating geospace. Adv Space Res 41(1):210–216. https://doi.org/10.1016/j.asr.2006.10.008
GCOS (2022) The 2022 GCOS implementation plan, World Meteorological Organization. Technical report, GCOS-244. https://gcos.wmo.int/site/global-climate-observing-system-gcos/publications
Grombein T, Lasser M, Arnold D, Meyer U, Jäggi A (2022) Determination and combination of monthly gravity field time series from kinematic orbits of GRACE, GRACE-FO and Swarm. In: Freymueller JT, Sánchez L (eds) Geodesy for a Sustainable Earth, IAG Symposia, vol 154, pp 191–201, https://doi.org/10.1007/1345_2022_163
Gunter BC, Encarnação J, Ditmar P, Klees R (2011) Using satellite constellations for improved determination of Earth's time-variable gravity. J Spacecr Rocket 48(2):368–377. https://doi.org/10.2514/1.50926
Guo X, Ditmar P, Zhao Q, Xiao Y (2020) Improved recovery of temporal variations of the Earth's gravity field from satellite kinematic orbits using an epoch-difference scheme. J Geod 94:69. https://doi.org/10.1007/s00190-020-01392-6
Humphrey V, Rodell M, Eicker A (2023) Using satellite-based terrestrial water storage data: a review. Surv Geophys 44(5):1489–1517. https://doi.org/10.1007/s10712-022-09754-9
Jäggi A, Arnold D (2017) Precise orbit determination. In: Naeimi M, Flury J (eds) Global Gravity Field Modeling from Satellite-to-Satellite Tracking Data, Lecture Notes in Earth System Sciences, pp 35–80, https://doi.org/10.1007/978-3-319-49941-3_2
Jäggi A, Hugentobler U, Beutler G (2006) Pseudo-stochastic orbit modeling techniques for low-Earth orbiters. J Geod 80(1):47–60. https://doi.org/10.1007/s00190-006-0029-9
Jäggi A, Dach R, Montenbruck O, Hugentobler U, Bock H, Beutler G (2009) Phase center modeling for LEO GPS receiver antennas and its impact on precise orbit determination. J Geod 83(12):1145–1162. https://doi.org/10.1007/s00190-009-0333-2
Jäggi A, Meyer U, Beutler G, Prange L, Mervart L (2011) AIUB-GRACE03S: A static gravity field model computed with simultaneously solved-for time variations from 6 years of GRACE data using the Celestial Mechanics Approach. Available from the International Centre for Global Earth Models, http://icgem.gfz-potsdam.de
Jäggi A, Dahle C, Arnold D, Bock H, Meyer U, Beutler G, van den IJssel J (2016) Swarm kinematic orbits and gravity fields from 18 months of GPS data. Adv Space Res 57(1):218–233. https://doi.org/10.1016/j.asr.2015.10.035
Jäggi A, Meyer U, Lasser M, Jenny B, Lopez T, Flechtner F, Dahle C, Förste C, Mayer-Gürr T, Kvas A, Lemoine JM, Bourgogne S, Weigelt M, Groh A (2020) International Combination Service for Time-Variable Gravity Fields – Start of operational phase and future perspectives. In: Freymueller JT, Sánchez L (eds) Beyond 100: The next Century in Geodesy, IAG Symposia, vol 154, pp 57–65, https://doi.org/10.1007/1345_2020_109
Jales P, Cartwright J, Talpe M, Mashburn J, Yuasa T, Nogues-Correig O, Nguyen V, Freeman V (2023) Spire Global's operational GNSS-reflectometry constellation for Earth surface observations. In: IGARSS 2023 – 2023 IEEE International Geoscience and Remote Sensing Symposium, IEEE, pp 884–887, https://doi.org/10.1109/IGARSS52108.2023.10282940
Johnstone A (2020) CubeSat design specification (1U-12U) rev 14 CP-CDS-R14. In: The CubeSat Program, Cal Poly SLO. https://www.cubesat.org/s/CDS-REV14_1-2022-02-09.pdf
Kobel C, Kalarus M, Arnold D, Jäggi A (2024) Impact of incorporating Spire CubeSat GPS observations in a global GPS network solution. Adv Space Res 73(12):6079–6093. https://doi.org/10.1016/j.asr.2024.04.015

Kopacz JR, Herschitz R, Roney J (2020) Small satellites an overview and assessment. Acta Astronaut 170:93–105. https://doi.org/10.1016/j.actaastro.2020.01.034

Kvas A, Behzadpour S, Ellmer M, Klinger B, Strasser S, Zehentner N, Mayer-Gürr T (2019) ITSG-Grace2018: overview and evaluation of a new GRACE-only gravity field time series. J Geophys Res Solid Earth 124(8):9332–9344. https://doi.org/10.1029/2019JB017415

Landerer FW, Flechtner FM, Save H, Webb FH, Bandikova T, Bertiger WI, Bettadpur SV, Byun SH, Dahle C, Dobslaw H, Fahnestock E, Harvey N, Kang Z, Kruizinga GLH, Loomis BD, McCullough C, Murböck M, Nagel P, Paik M, Pie N, Poole S, Strekalov D, Tamisiea ME, Wang F, Watkins MM, Wen HY, Wiese DN, Yuan DN (2020) Extending the global mass change data record: GRACE Follow-On instrument and science data performance. Geophys Res Lett 47(12):e2020GL088306. https://doi.org/10.1029/2020GL088306

Lasser M (2023) Noise modelling for GRACE Follow-On observables in the Celestial Mechanics Approach. PhD thesis, Geodätisch-geophysikalische Arbeiten in der Schweiz, vol 110, Schweizerische Geodätische Kommission. https://www.sgc.ethz.ch/sgc-volumes/sgk-110.pdf

Liu Y, Li J, Xu X, Wei H, Li Z, Zhao Y (2024) Simulation analysis of recovering time-varying gravity fields based on starlink-like constellation. Geophys J Int 239(1):402–418. https://doi.org/10.1093/gji/ggae273

Lyard FH, Allain DJ, Cancet M, Carrère L, Picot N (2021) FES 2014 global ocean tide atlas: design and performance. Ocean Sci 17(3):615–649. https://doi.org/10.5194/os-17-615-2021

Meyer U, Sosnica K, Arnold D, Dahle C, Thaller D, Dach R, Jäggi A (2019) SLR, GRACE and Swarm gravity field determination and combination. Remote Sens 11(8):956. https://doi.org/10.3390/rs11080956

Petit G, Luzum B (2010) IERS Conventions 2010. IERS Technical Note 36, Verlag des Bundesamts für Kartographie und Geodäsie, Frankfurt am Main, Germany, https://www.iers.org/IERS/EN/Publications/TechnicalNotes/tn36.html

Pfaffenzeller N, Pail R (2023) Small satellite formations and constellations for observing sub-daily mass changes in the Earth system. Geophys J Int 234(3):1550–1567. https://doi.org/10.1093/gji/ggad132

Reigber C, Lühr H, Schwintzer P (2002) CHAMP mission status. Adv Space Res 30(2):129–134. https://doi.org/10.1016/S0273-1177(02)00276-4

Richter H, Lück C, Klos A, Sideris M, Rangelova E, Kusche J (2021) Reconstructing GRACE-type time-variable gravity from the Swarm satellites. Sci Rep 11(2):1117. https://doi.org/10.1038/s41598-020-80752-w

Rummel R, Balmino G, Johannessen J, Visser P, Woodworth P (2002) Dedicated gravity field missions – principles and aims. J Geodyn 33(1):3–20. https://doi.org/10.1016/S0264-3707(01)00050-3

Schreiter L, Brack A, Männel B, Schuh H, Arnold D, Jäggi A (2024) Imaging of the ionosphere and plasmasphere using GNSS slant TEC obtained from LEO satellites. Radio Sci 59(12):e2024RS008058. https://doi.org/10.1029/2024RS008058

Švehla D, Rothacher M (2005) Kinematic precise orbit determination for gravity field determination. In: Sansò F (ed) A Window on the Future of Geodesy, IAG Symposia, vol 128, pp 181–188, https://doi.org/10.1007/3-540-27432-4_32

Tapley BD, Bettadpur S, Watkins M, Reigber C (2004) The gravity recovery and climate experiment: mission overview and early results. Geophys Res Lett 31(9):L09607. https://doi.org/10.1029/2004GL019920

Tapley BD, Watkins MM, Flechtner F, Reigber C, Bettadpur S, Rodell M, Sasgen I, Famiglietti JS, Landerer FW, Chambers DP, Reager JT, Gardner AS, Save H, Ivins ER, Swenson SC, Boening C, Dahle C, Wiese DN, Dobslaw H, Tamisiea ME, Velicogna I (2019) Contributions of GRACE to understanding climate change. Nat Clim Chang 9(5):358–369. https://doi.org/10.1038/s41558-019-0456-2

Teixeira da Encarnação J, Visser P, Arnold D, Bezdek A, Doornbos E, Ellmer M, Guo J, van den IJssel J, Iorfida E, Jäggi A, Klokocník J, Krauss S, Mao X, Mayer-Gürr T, Meyer U, Sebera J, Shum CK, Zhang C, Zhang Y, Dahle C (2020) Description of the multi-approach gravity field models from Swarm GPS data. Earth Syst Sci Data 12(2):1385–1417. https://doi.org/10.5194/essd-12-1385-2020

van Gelderen M, Koop R (1997) The use of degree variances in satellite gradiometry. J Geod 71(6):337–343. https://doi.org/10.1007/s001900050101

Wahr J, Molenaar M, Bryan F (1998) Time variability of the Earth's gravity field: hydrological and oceanic effects and their possible detection using GRACE. J Geophys Res Solid Earth 103(B12):30205–30229. https://doi.org/10.1029/98JB02844

Weigelt M, Dam T, Jäggi A, Prange L, Tourian MJ, Keller W, Sneeuw N (2013) Time-variable gravity signal in Greenland revealed by high-low satellite-to-satellite tracking. J Geophys Res Solid Earth 118(7):3848–3859. https://doi.org/10.1002/jgrb.50283

Weigelt M, Jäggi A, Meyer U, Arnold D, Mayer-Gürr T, Öhlinger F, Sośnica K, Ebadi S, Schön S, Steffen H (2024) Bridging the gap between GRACE and GRACE-Follow-On by combining high-low satellite-to-satellite tracking data and satellite laser ranging. J Geod 98:84. https://doi.org/10.1007/s00190-024-01888-5

Wu SC, Yunck TP, Thornton CL (1991) Reduced-dynamic technique for precise orbit determination of low Earth satellites. J Guid Control Dyn 14(1):24–30. https://doi.org/10.2514/3.20600

Zhong L, Sósnica K, Weigelt M, Liu B, Zou X (2021) Time-variable gravity field from the combination of HLSST and SLR. Remote Sens 13(17):3491. https://doi.org/10.3390/rs13173491

Zhou H, Zhou Z, Luo Z, Wang K, Wei M (2020) What can be expected from GNSS tracking of satellite constellations for temporal gravity field model determination? Geophys J Int 222(1):661–677. https://doi.org/10.1093/gji/ggaa177

Zingerle P, Gruber T, Pail R, Daras I (2024) Constellation design and performance of future quantum satellite gravity missions. Earth Planets Space 76:101. https://doi.org/10.1186/s40623-024-02034-3

Zumberge JF, Heflin MB, Jefferson DC, Watkins MM, Webb FH (1997) Precise point positioning for the efficient and robust analysis of GPS data from large networks. J Geophys Res Solid Earth 102(B3):5005–5017. https://doi.org/10.1029/96JB03860